Received August 25, 2018, accepted September 26, 2018, date of publication October 1, 2018, date of current version October 25, 2018.

*Digital Object Identifier 10.1109/ACCESS.2018.2873278*

# Bidirectional Mode Slicing and Re-Combining for Mode Conversion in Planar Waveguides

**EHAB AWAD, (Senior Member, IEEE)**
Electrical Engineering Department, College of Engineering, King Saud University, Riyadh 11421, Saudi Arabia
e-mail: esawad@ieee.org

This work was supported in part by the Research Center at the College of Engineering and in part by the Deanship of Scientific Research at King Saud University.

**ABSTRACT** Photonics integrated circuits and planar lightwave circuits are crucial in future high capacity optical communication networks. Such circuits can perform complicated and sophisticated signal processing functions' on-chip level. However, they should have high bandwidth in order to handle ultrafast data flow and thus achieve high-capacity transmission. One way to achieve such high bandwidth is using few-mode waveguides. Therefore, it becomes mandatory to find a way to convert from current conventional single-mode planar waveguides into few-mode waveguides, and moreover to selectively excite the desired modes within the converted multimode waveguides. In this paper, a novel silica-glass planar waveguide converter is numerically demonstrated for the first time. This device can convert in a bidirectional fashion between single-mode and two, three, or four modes planar waveguides, in addition, to selectively excite the desired mode. The device principle of operation mainly depends on spatial modes slicing and re-combining to achieve the desired higher or lower order modes. That could be accomplished by cascading stages of V-shape and M-shape graded-index planar waveguides. The graded-indices allow for flexible and simple geometrical designs that can split or combine fundamental as well as higher order modes. The finite-difference time-domain numerical method is utilized to verify the device operation and evaluate its performance for each excited mode in bidirectional directions. The device shows good performance over the entire C-band wavelength range with the worst-case magnitude of insertion-loss $\cong$ 3 dB, polarization-dependent loss $\cong$ 0.6 dB, and return-loss $\cong$ 21 dB. It also shows a worst-case cross-talk of $\cong -24.1$ dB among the excited high-order modes in the forward direction, and a worst-case mode-rejection ratio of $\cong -23$ dB for non-excited modes in the reverse direction. Moreover, the device shows reasonable performance tolerance to variations in V-shape and M-shape waveguide design parameters.

**INDEX TERMS** Optical communications, photonic integrated circuits.

## I. INTRODUCTION

Photonics integrated circuits (PIC) and planar lightwave circuits (PLC) with large bandwidth are essential in high capacity optical communication networks. They are crucial to perform ultrafast optical signal processing operations without sacrificing the networks high-capacity. One way to achieve that on single-mode propagating signals is to combine different techniques such as time-division-multiplexing, wavelength-division-multiplexing (WDM), polarization-division-multiplexing, and complex modulation formats. Another way is to convert single-mode signals into multi-mode signals and then multiplex them together over multi-mode waveguides using mode-division-multiplexing in order to handle high aggregate data rates (i.e. large bandwidth).

The silica-glass material is used to be an attractive choice for planar waveguide based devices, which are designed for optical communication applications. That is because silica-glass has some unique features like relatively low optical loss and nonlinearities, especially over the optical communication wavelength range. Besides, it is compatible with silica-based planar integrated circuits and planar lightwave circuits as well as standard optical fibers. In other words, it does not mandates using long adiabatic tapers or spot-size matching converters at device inputs or outputs, as the case with silicon photonic technology devices, when they are connected to optical fibers. In addition, silica-glass offers physical and chemical stability, reliability, ease of fabrication, high thermo-optical coefficient, and low cost [1]–[3]. Different optical components

have been realized using silica-glass PLC technology such as directional couplers, variable optical attenuators, Mach-Zehnder interferometers, arrayed waveguide gratings, and reconfigurable optical add-drop multiplexers [2], [4]–[6]. Moreover, coherent receivers, optical orthogonal frequency division multiplexer, and highly functional modulators have been also demonstrated [1]. Furthermore, silica-glass power Y-splitter for multicore optical fiber was demonstrated using space-division-splitting technique [7], and graded-index 'V' power-splitter was realized using silica-glass material [8].

Different techniques have been reported on mode conversions in planar waveguides. For example, two modes excitation in a few-modes waveguide using Mach-Zehnder interferometer was demonstrated [9], [10]. In which, the mode conversion and exchange were demonstrated for two-mode waveguides. Also, an optical mode converter using tapered waveguide splitters was demonstrated at a single wavelength of 1550nm [11]. In that work, the conversion between TE0 and TE3 in addition to TE1 and TE2 are illustrated, with an estimated cross-talk of $\cong$ 11.4dB. A symmetric and asymmetric Y-junctions have been proposed for few-modes and multimode excitation [12]. In which, the performance of mode conversion was dependent on fine-tuning of taper-angle between the Y-junction arms.

Although the main focus in this work here is planar waveguides mode conversion, it is worth also to mention some techniques on mode-division-multiplexing (MDM) as one possible potential application for such mode-conversion. Different techniques have been reported on on-chip MDM. For example, data exchange of MDM TE0 and TE1 modes has been demonstrated using silicon-on-insulator (SOI) micro-ring resonators for use in flexible networks [13]. An SOI on-chip MDM for TE0 and TE1 modes plus WDM switch were demonstrated using single-mode elements [14]. On-chip two-modes MDM using SOI tapered directional couplers was also demonstrated [15]. On-chip simultaneous MDM and polarization division multiplexing were demonstrated using densely packed waveguide array [16]. All these techniques involve conversion to or between few-mode waveguides that can handle up to two modes. However, in [17], an SOI mode multiplexer was demonstrated using asymmetric directional couplers. It could handle up to four modes at the same polarization. It showed a good performance only over the 20nm tunable single-carrier wavelength range, and fabrication tolerance of $\pm$10nm. Although the device was short because of using silicon technology, however, it was still mandatory to use relatively long adiabatic mode-size converters at the device inputs and outputs to achieve good performance, otherwise, the total insertion losses from fiber-to-fiber could reach up to 12-13dB.

Here in this work, and for the first time, a novel planar silica-glass waveguide converter (WGC) device is proposed and numerically demonstrated. The device can convert in bi-directional directions from conventional single-mode waveguide (1M-WG) to three or four modes waveguide (3M/ 4M-WG) by going through an intermediate stage of two modes waveguides (2M-WG). The device can be designed to selectively excite one desired mode inside the output few-modes waveguides. The selective mode excitation (or conversion) between 1M-WG and 3M/ 4M-WG is based on slicing of input mode spatially into four quarters.

All quarters have the same power, however, each one has its own unique phase. The quarters' phases are then adjusted independently before re-combining them again to achieve the desired output mode. The mode slicing and re-combining are performed using V-shape and M-shape graded-index (GI) slicers and combiners. The V-shape GI profiles make sharp deflections to propagating signal beams, while the M-shape GI profiles make more gentle deflections. The V-shape mode slicer/ combiner is more suitable for deflections of single-beam quarters (e.g. TE0 mode), while the M-shape mode slicer/ combiner is more suitable for deflections of double-beam quarters (e.g. TE1 mode). It is well known that conventional step-index Y-splitters or combiners are commonly used with fundamental modes only, and mandate very careful and critical design of waveguides branching angles and adiabatic tapering. On contrary, the GI designs here allow for dealing with fundamental (TE0) as well as higher order modes (TE1, TE2, or TE3), while preserving their beam confinement profile during propagation. Also, the GI allows for flexible non-critical geometrical designs, such as different possible tilting (apex) angles for the V-shape waveguides, and M-shape GI planar WG. The three dimensional (3D) finite difference time domain (FDTD) simulations throughout this work verify the WGC operation in bidirectional directions for each excited mode, and they also illustrate good device performance over the entire C-band wavelength range for all tested cases.

## II. PRINCIPLES OF OPERATION

Fig. 1 (a) shows the schematic structure of a planar silica-glass waveguide converter (WGC) device. It consists of three stages of mode slicers (MS) and mode combiners (MC). The WGC can convert from a single-mode (1M) waveguide (WG) into three-mode (3M) or four-mode (4M) waveguides and vice versa. The device together with its input and output WGs are all surrounded by a cladding region having a refractive index of 1.45. The first stage converts from input 1M-WG into two-mode (2M) waveguides and thus slices input fundamental mode (TE0) into two equal-power fundamental modes (TE0). The second stage has two input 2M-WGs and also two output 2M-WGs. It slices each input M-WG fundamental mode in two equal-power halves in order to have overall of four equal-power quarters for the original input single-mode. However, each quarter has its own original phase. The second stage re-adjusts the phase differences among different quarters by introducing appropriate '$\pi$' phase shifts among them. Then, it re-combines every two quarters to selectively excite the desired mode (TE0 or TE1) into the output 2M-WGs. Finally, the third stage re-combines the two input modes coming from two input 2M-WGs in order to selectively excite the desired mode (TE0, TE1, or TE2) in

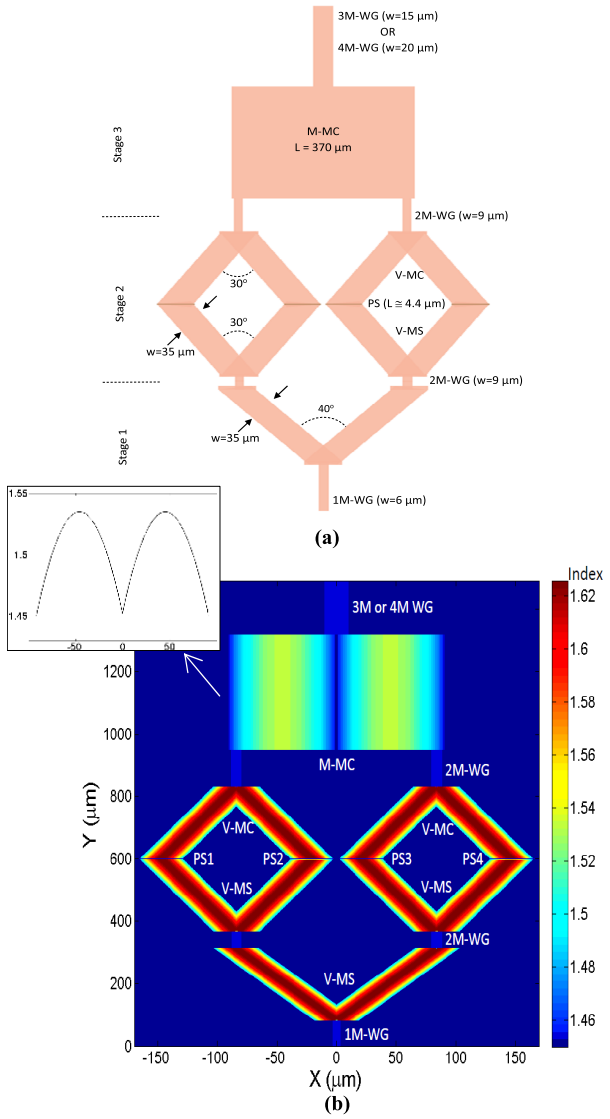


**FIGURE 1.** The silica-glass planar waveguide converter (WGC) device configuration. (a) The schematic structure, (b) The refractive-index distribution. The inset in (b) shows the M-shape index distribution within the third stage. The 1M, 2M, 3M, and 4M–WG corresponds to single, two, three, and four-mode waveguides, respectively. The V-MS/ C is the V-shape graded-index mode-slicer/ combiner. The M-MC is the M-shape graded-index mode-combiner. PS: phase-shifter, L: waveguide length, and W: waveguide width.

the output 3M-WG, or the desired mode (TE0, TE1, TE2, or TE3) in output 4M-WG.

Fig. 1 (b) shows the refractive-index distribution of planar silica-glass waveguides converter device. The first stage consists of V-shape mode-slicer (V-MS). The V-MS slices input fundamental-mode of 1M-WG, and splits its power into fundamental-modes of the two output 2M-WG. The VMS consists of two angle-tilted waveguides each at $20^{o}$ with respect to input core central-axis. Thus, the two waveguides form a V-shape with a total apex angle of $40^{o}$. Each of the V-shape planar waveguides has a width W $= 35\mu$m. The input core is placed at the location of V-shape apex tip in order to have a symmetrical input mode slicing, and thus 50:50 power splitting ratio. The two output 2M-WG cores are aligned at the WGs outputs in order to selectively excite their fundamental modes. The separation between the output cores is $\cong 168\mu$m. The 1M-WG and 2M-WG cores are selected to have a refractive index of $n_c = 1.4551$. The 1M-WG core width is $6\mu$m, and the output 2M-WG cores width is $9\mu$m. Whereas the height of all waveguides of the WGC device is 6 $\mu$m. Each waveguide of V-MS has a parabolic graded index (GI) distribution spanning the entire WG width with a peak index ($n_o$) centered at the waveguide central-axis. The parabolic GI profile can be expressed [18] as:

$$n(w) = n_o\left(1 - \frac{1}{2}\alpha^2 w^2\right) \tag{1}$$

Where $n_o = 1.63$ and $\alpha_V = 3.1 \times 10^{-2}\ \mu m^{-1}$. The input and output cores tips are designed to have conical shapes with an apex-angle of $164^{o}$ in order to reduce the induced back-reflections at the interface between input/ output cores and the GI waveguides. The back-reflections mainly result from the relatively large index difference between V-shape waveguides and cores. The input 1M-WG fundamental mode sees a symmetric overlapping area between the numerical-apertures (NA) of tilted WGs. Thus, the mode is sliced by half, and each half propagates into one WG. These WGs numerical-aperture can be expressed [18] as:

$$NA = n_c \sin\theta_a \cong n_o \alpha W/2 \tag{2}$$

Where '$\theta_a$' is the acceptance angle seen at the WG input. The calculated acceptance angle from Eq. (2) is $\theta_a \cong 28.41^{o}$. The angle-tilted waveguides allow oblique incidence of each splitted beam at $20^{o}$ with respect to each WG central-axis. Thus, the input core beam falls within the overlapping area between the numerical-apertures of the two WGs, and therefore its power is splitted by 50:50 between WGs, as illustrated later in Fig. 2. Each splitted beam deflects by double the tilting angle $\cong 2\times 20^{o} = 40^{o}$ (measured with respect to input core central-axis), after the first total internal reflection (TIR) on the waveguide side-wall. Then, each deflected beam propagates confined inside its WG and hits the other side-wall to deflect again by TIR at an angle $\cong -40^{o}$. Thus, it finally emerges from the WG output parallel to the input beam direction. The sliced mode beam is launched at the center of output 2M-WG to ensure excitation of its fundamental mode. The choice of V-MS GI profile parameters and tilt-angle are made to have splitting and deflections within a relatively short distance without much radiation loss into the cladding. The choice of parabolic GI profile results in a confined beam propagation throughout WGs without excitation of higher-order modes, and thus ensures direct fundamental mode-matching at the output 2M cores.

It is worth mentioning that the choice of $20^{o}$ tilting-angle here ensures that it is small enough than the acceptance angle '$\theta_a$' to minimize radiation mode losses into cladding. Also, it is small enough to reduce the relative V-MS width

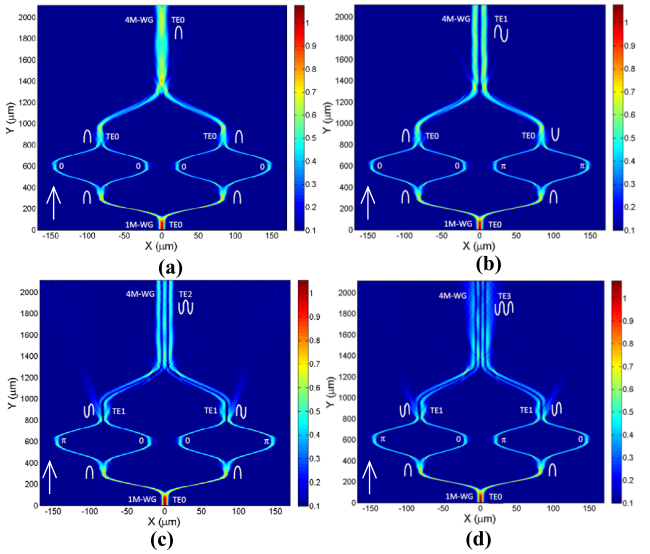


**FIGURE 2.** The FDTD simulations of electric field magnitudes in a.u. (x-y cross-sections) for the case of WG conversion from 1M-WG to 4M-WG in the forward direction. The phase-shifters are adjusted in each case to selectively excite: (a) TE0, (b) TE1, (c) TE2, and (d) TE3 mode in the output 4M waveguide. The propagating modes are sketched at each stage. The white arrow on the lower-left corner indicates the propagation direction.

($\cong 168\mu$m), and thus give more margin to possible fabrication errors. However, the choice of 20° is also considered large enough to reduce the relative V-MS waveguide length ($\cong 245\mu$m) and thus the overall WGC device size, as well. Of course, the designed length of the V-MS depends on the TIR path inside the graded-index waveguides. The $245\mu$m waveguide length of V-MS is selected to ensure that the deflected output beams from WGs returns back confined and in a parallel direction with the input beam, as shown later in Fig. 2. To achieve such optimized length, each output 2M-WG are aligned along both 'x' and 'y' directions until the output beams match TE0 fundamental mode of the 2M-WGs. Which in turn, minimizes the V-MS overall insertion loss. After optimization, it is found that the separation between the outputs 2M-WGs cores is $\cong 168\mu$m.

The second stage consists of two side-by-side and parallel V-shape mode slicers and combiners (MS, and MC). Each MS-MC forms a diamond-like structure (shape), as shown in Fig. 1. The MS-MC receives the two sliced fundamental modes out of the first stage and slices them again into four quarters of equal-power beams using two separate V-MS. The two V-MS configuration and operation are exactly the same like that of the first stage V-MS, except that the tilting angles of V-shaped waveguides here are 15° with a total apex angle of $2 \times 15^{o} = 30^{o}$. Of course, the tilting angles are selected here also according to Eq. (1) to be less than $\theta_a$. However, the 15° is chosen to be small enough to ensure that the two parallel MS-MC diamond shapes come side-by-side with a center-to-center separation of $\cong 168\mu$m (i.e. equals to previous stage output 2M-WGs separation). In the meanwhile, the 15° allows having a safety margin separation between diamond shapes edges of $\cong 10\mu$m in order to overcome possible fabrication errors. In addition, the 15° is still considered large enough to reduce the overall second stage length ($\cong 460\mu$m). It is also worth mentioning that the different choices of V-MS apex angles of the first and second stages (i.e. 20° and 15°) did not affect the V-MS operation or performance, which proves the flexibility and non-critical angle design of GI V-shape slicers.

Each V-MS is followed by a V-shape mode combiner (V-MC) in order to re-combine the four single-beams quarters again before the two output 2M-WG. The two V-MC combiners operate and have configuration exactly the same like V-MS of this stage, except that they work in the reverse direction. Thus, each V-MC can re-combine two input beams into one output beam. Again, as stated earlier, the lengths of each V-MS and V-MC in diamond structures are optimized to ensure that deflected beams come back by TIR parallel to input beams and also to best-match the modes of output 2M-WGs in order to minimize insertion loss. There are four phase-shifters (PS1 through PS4) placed in between the V-MS and V-MC in order to modify the relative phase differences among the four quarters beams before recombination. Thus, every two re-combined beams can selectively excite the desired mode in each output 2M-WG. The phase-shifters (PS) are designed to introduce either '0' or '$\pi$' phase-shifts for each propagating quarter mode in order to re-adjust the relative phase differences among quarters and thus excite the desired output mode. The phase shifters operation is governed by the following equation [18]:

$$\Delta\phi = 2\pi L \Delta n/\lambda_o \tag{3}$$

All phase-shifters have the same length, L $\cong 4.4\mu$m. It is worth mentioning that the phase shifters here are static and can be considered as step-index short waveguides separating between the V-MS and V-MC sections. The phase-shift ($\Delta\phi$) is adjusted by selecting the refractive-index of the phase shifter to be either 1.63 for a zero-phase shift (i.e. equals to GI peak value), or 1.4551 for $\pi$-phase shift. Therefore, for $\Delta\phi = \pi$, the refractive index difference is $\Delta$n = 1.63-1.4551 = 0.1749. The '$\lambda_o$' is the propagating light wavelength, where the phase shifters are designed to operate in the C-band range (i.e. $\lambda_o$ =1.53 to 1.565 $\mu$m). Due to different wavelengths values across the C-band, there could be a possible deviation in $\Delta\phi$ selected value. This $\Delta\phi$ is found to be $\cong \pm$ 1.1%, which is considered small and does not affect the device performance, as will be discussed later. Also, according to Eq. (3), a deviation in refractive index difference $\Delta$n between phase-shifters (i.e. possible index mismatch) of $\cong \pm 0.0019$, for example, can result in a same acceptable deviation in $\Delta\phi \cong \pm 1.1\%$. However, it is worth mentioning that using thermo-optic thin film heaters [4], [5] could be useful to fine tune the selected static phases in order to achieve accurate phase differences among sliced mode quarters, or alternatively, switch the refractive-index in order to achieve dynamic phase shifters.

The third stage consists of an M-shape mode combiner (M-MC). The M-shape graded-index profile consists of

two parabolas side-by-side with a minimum index value almost equals to the device cladding index, as shown in Fig. 1 (b) inset. The minima are located at the middle and boundaries of M-MC waveguide. Thus forming together an M-shape across the waveguide entire width. The waveguide average width is $W_M \cong 179\mu$m, and its length is $L_M \cong 370\mu$m. According to Eq. (1), each parabolic profile has a peak index value $n_o = 1.535$ and $\alpha_M = 8.5 \times 10^{-3}\mu m^{-1}$. It is worth mentioning that the M-shape might be viewed as a special case of V-shape with zero apex angle, and thus it looks like one big planar waveguide. That proves the flexibility of GI slicer/ combiner designs that can function well at different selected apex angles, depending on the geometrical design requirements and available space.

The third stage receives the two input modes out of the second stage and re-combines them together into one output mode in either 3M or 4M-WG. The separation between the third stage two inputs 2M-WGs is already set by the previous stage at $\cong 168\mu$m. The selected output 3M-WG and 4M-WG core widths are $15\mu$m and $20\mu$m, respectively, and they are positioned at the M-shape profile center. Each input beam is deflected by TIR twice at the boundaries of each parabolic GI profile while propagating toward the output waveguide, as illustrated later in Fig. 2. In the case of 4M-WG, it is found that the best M-MC width to excite even modes (TE0 & TE2) in output waveguide is $W = 178\mu$m, while the best width to excite the odd modes (TE1 & TE3) is $W = 182\mu$m. Whereas, in the case of 3M-WG, the best M-MC width to excite the even modes (TE0 & TE2) in output waveguide is $W = 177\mu$m, while the best width to excite the odd mode TE1 is $W = 180\mu$m. That is because the odd-modes distributions inside output few-mode waveguide are usually shifted laterally by few microns with respect to even-modes. Therefore, we can say for each case of 3M or 4M-WG we have two optimized M-shape width designs, one for odd-modes excitation and the other for even modes excitation. The M-MC widths and lengths are selected and optimized to minimize the insertion loss of desired excited mode as well as to minimize its cross-talk with other undesirable excited modes. As the input and output waveguide positions of the third stage are already determined, the M-shape waveguide width and length were tuned in sub-micron steps along the 'x' and 'y' directions, while monitoring the insertion loss for each excited mode in the output 3M or 4M-WG. The width and length are optimized to minimize the insertion loss of the desired excited mode, which in turn maximizes the insertion loss of undesired modes (i.e. minimizes cross-talk). More discussions about the optimized WGC device insertion losses and cross-talks are given later in the performance evaluation section.

The M-shape GI profile is found to be more appropriate than V-shape profile for combining TE1 modes (or slicing higher-order modes into TE1 mode, as shown later), because TE1 propagates as two side-by-side parallel beams and thus the M-shape preserves TE1 beams parallelism as well as separation at waveguide output, i.e. it does not introduce distortion. The following simple mathematical derivation illustrates that more.

Generally, the beam propagation through a graded-index profile can be described by the Eikonal differential equation [18]:

$$\frac{d^2w}{dL^2} = \frac{1}{n(w)}\frac{dn(w)}{dw} \tag{4}$$

Where 'w' is the width of the GI profile. The $w = 0$ is located at GI peak value '$n_o$', and 'L' is the propagation length along the GI waveguide. Substituting Eq. (1) into Eq. (4) and solving for the beam path trajectory along the waveguide, we get the following two sinusoidal solutions that approximately describe the output beam position '$w_{out}$' and angle '$\theta_{out}$' as functions of input beam position '$w_{in}$' and angle '$\theta_{in}$':

$$w_{out} \cong w_{in}cos(\alpha L) + \frac{\theta_{in}}{\alpha}sin(\alpha L) \tag{5}$$

$$\theta_{out} = \frac{dw_{out}}{dL} \cong -w_{in}\alpha sin(\alpha L) + \theta_{in}cos(\alpha L) \tag{6}$$

The 'w' and 'L' are measured in '$\mu$m'. The input or output angles are measured between propagating beam direction and the normal to waveguide input or output interface. Let's assume that the TE1 two parallel beams enter GI waveguide at two points located at '$w_{in1}$' and '$w_{in2}$'. Therefore, the difference $\Delta w_{in} = w_{in1} - w_{in2}$ should be kept the same at waveguide output (i.e. $\Delta w_{out} = w_{out1} - w_{out2}$) in order to excite the desired modes in output cores. Also, the difference between parallel beams angles at waveguide input $\Delta\theta_{in} = \theta_{in1} - \theta_{in2} = 0$ should be kept the same at waveguide output in order to preserve parallelism. Therefore, from Eq. (5) and Eq. (6), respectively:

$$\Delta w_{out} = w_{out1} - w_{out2} = \Delta w_{in}cos(\alpha L) \tag{7}$$

$$\Delta\theta_{out} = \theta_{out1} - \theta_{out2} = -\Delta w_{in}\alpha sin(\alpha L) \tag{8}$$

For M-shape GI, $\theta_{in1} = \theta_{in2} = 0$ at the waveguide input, as shown later in Fig. 2. Also, $L_M = \pi/\alpha_M = 370\mu$ m. Therefore, $\Delta w_{out} = -\Delta w_{in}$, which means the beams' separation is maintained at waveguide output. Also, $\Delta\theta_{out} = 0$, which means the beams are still parallel. Moreover, the gentle slope '$\alpha_M$' of M-shape reduces the frequency of sinusoidal expressions and thus the sharpness of beams deflections. That, in turn, facilitates collection and matching between output TE1 parallel beams and the desired output cores modes. Hence, the choice of M-shape with gentle '$\alpha_M$' and appropriate '$L_M$' is suitable for TE1 modes propagation.

For V-shape GI, $\theta_{in1} = \theta_{in2}$ equals to the waveguides tilting angle (i.e. $15^o$ or $20^o$). The waveguide length is $L_V \cong 245\mu$m, which is much greater than $\pi/\alpha_V = 101.34\ \mu$m. Therefore for TE1, $\Delta w_{out} = 0.26 \times \Delta w_{in}$, which means the beams separation will be reduced at waveguide output. Also, $\Delta\theta_{out} = -0.03 \times \Delta w_{in} \neq 0$, which means the beams will not be parallel anymore at waveguide output. However, for a single-mode beam (e.g. TE0) that does not impose a problem at all. Therefore, the sharp slope '$\alpha_V$' of

V-shape becomes advantageous as it increases the frequency of sinusoidal expressions allowing for sharp beam deflections, and thus reduces the length of V-shape slicer (or combiner), which in turn reduces the overall device length.

Fig. 2 and Fig. 3 show the three-dimensional (3D) finite difference time domain (FDTD) simulations of the device electric fields in arbitrary units (a.u.) using Lumerical Solutions software [19]. It illustrates the conversion from 1M-WG to 4M-WG with selective mode excitations at the operating wavelength of 1550 nm. Fig. 2 show the two dimensional (2D) cross-sections (x-y directions) of 3D simulations for excitation of 1$^{st}$ (fundamental), 2$^{nd}$, 3$^{rd}$, and 4$^{th}$ order modes, respectively in the 4M-WG. The input fundamental mode of 1M-WG is propagating in the forward direction along the positive y-direction. Every change in the confined beam propagation direction (i.e. beams deflections) indicates a TIR inside the V-shape or M-shape GI waveguides. The white sinusoidal sketches illustrate the different propagating modes shapes. The phase difference between peaks and troughs is '$\pi$'. The introduced phase-difference

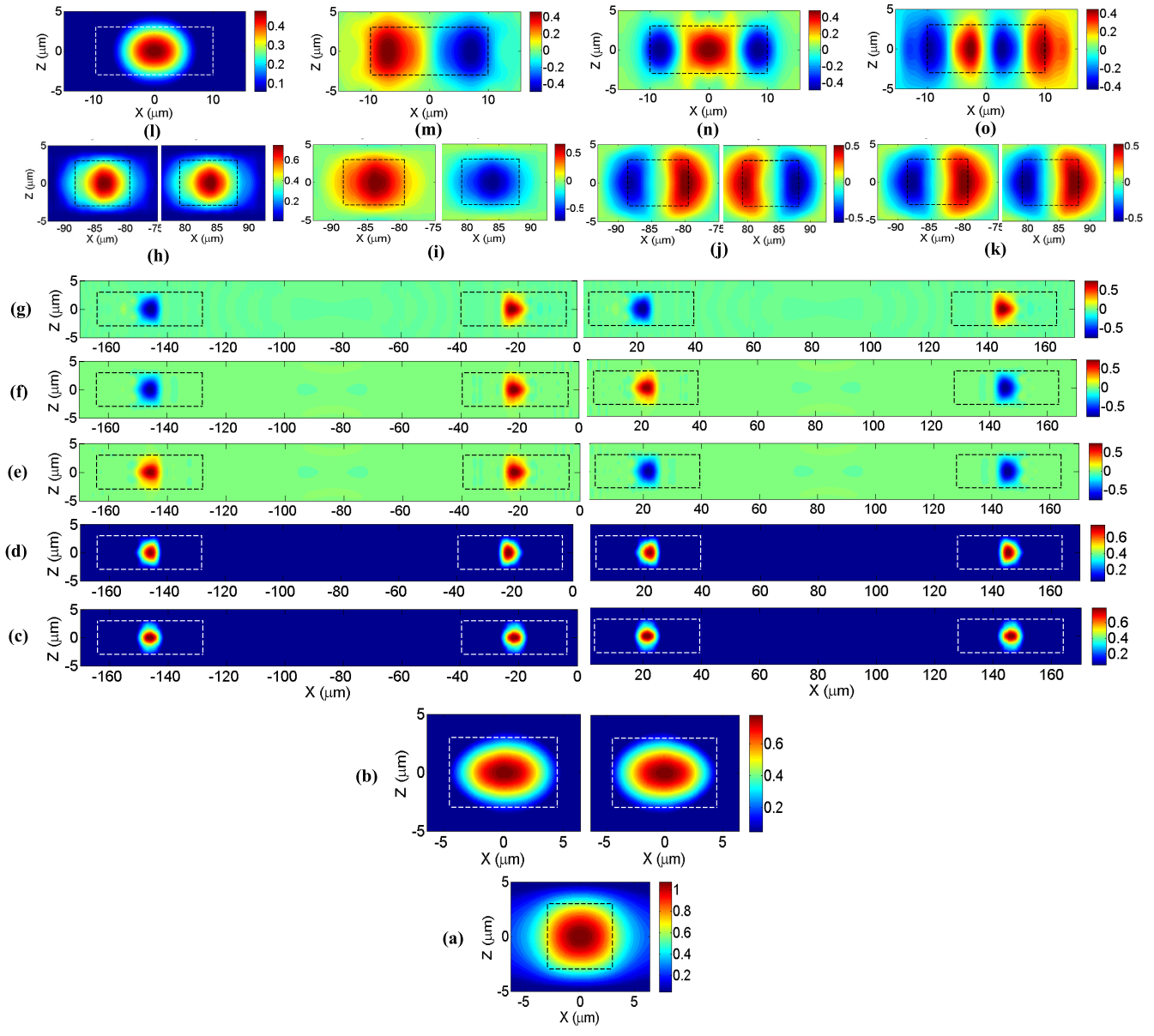


**FIGURE 3.** The FDTD simulations of mode-profiles electric fields in a.u. (x-z cross-sections) for the case of WG conversion from 1M-WG to 4M-WG in the forward direction. The dashed rectangles indicate waveguides cores boundaries. (a) Input TE0 mode-profile in 1M-WG of the first stage, (b) Output TE0 modes in left and right 2M-WGs of the first stage, respectively, (c) The TE0 mode-profiles inside left and right diamond structures waveguides, respectively, just before the phase-shifters. The TE0 mode-profiles inside the left and right diamond structures waveguides, respectively, just after the phase-shifters for different cases of conversion to (d) TE0, (e) TE1, (f) TE2, and (g) TE3 modes. The TE0 and TE1 mode-profiles in outputs left and right 2M-WGs of the second stage for different cases of conversion to (h) TE0, (i) TE1, (j) TE2, and (k) TE3 modes. The converted output mode-profiles in the 4M-WG for the case of (l) TE0, (m) TE1, (n) TE2, and (o) TE3 modes.

(0 or $\pi$) in each path is indicated based on each phase-shifter adjustment, in order to selectively excite the desired mode in the output few-modes waveguide. As clearly shown, the WGC slices the fundamental-mode of input single-mode waveguide twice, in two steps, to get four equal-power quarters. The relative phase differences among quarters are re-adjusted to synthesize one of the desired output waveguide modes. Then, the four quarters are re-combined, in two steps, to excite the output target mode. In order to excite the TE2 or TE3 modes in the output waveguide, we need to combine the two TE1 modes out of the second stage, as shown in Fig. 2 (c)-(d). However, each TE1 mode looks like two parallel propagating beams side-by-side. In order for TE1 modes to excite TE3 or TE4 at proper locations inside output waveguide, it is mandatory to gently deflect the TE1 two-beams by TIRs without distorting their parallelism, as explained earlier. This is why an M-shape mode combiner (M-MC) is used instead of V-shape combiner (V-MC) in the third stage. The M-MC graded index profile has a gentle parabolic slope (i.e. small '$\alpha_M$') and thus a wide mode combiner waveguide width, as indicated earlier and illustrated in Fig. 1.

Fig. 3 shows the two-dimensional cross-sections (x-z directions) of 3D simulations for propagating modes-profiles inside waveguides at some selected critical locations of different stages. The figure illustrates a step-by-step evolution of mode-profiles along the propagation direction, and thus verifies the device operation. The selected case for illustration here is a conversion from 1M-WG to 4M-WG in the forward direction, similar to the case in Fig. 2. The mode-profile electric-fields are represented in a.u. The dashed rectangles indicate the boundaries between waveguides cores and cladding. Fig. 3-a and 3-b illustrate the TE0 mode-profiles at the 1M-WG input and two 2M-WG outputs of the first stage. While Fig. 3-c illustrates the cross-sections of left and right diamond structures just before the phase-shifters. These cross-sections show TE0 modes, and they are applicable to all cases of conversions. Fig. 3-d, 3-e, 3-f, and 3-g illustrate the cross-sections of left and right diamond structures just after the phase-shifters. They correspond to conversion to output TE0, TE1, TE2, and TE3 modes, respectively. Fig. 3-h, 3-i, 3-j, and 3-k illustrate TE0 and TE1 mode-profiles at output 2M-WGs of the second stage, corresponding to conversions to output TE0, TE1, TE2, and TE3 modes, respectively. Fig. 3-l, 3-m, 3-n, and 3-o illustrate mode-profiles at the output 4M-WG of the third stage for the cases of conversions to TE0, TE1, TE2, and TE3 modes, respectively.

All such mode profiles in Fig. 3 show good quality shapes and conversions. These profiles are also used in the characterization and performance evaluation of the device, through numerical mode overlap integrals [19]. They are used to estimate insertion-loss, cross-talk, as well as mode-rejection ratio in reverse direction, as discussed later.

Similarly, the case would be for conversion from 1M-WG to 3M-WG. Therefore, it is found to be sufficient showing the case of 3D FDTD of 4M-WG as an example here. However, it is worth mentioning that the WGC converts to 3M or 4M WG through the intermediate second stage of 2M-WGs. Therefore the device inherently converts from 1M-WG to 2M-WG in the second stage.

Fig. 4 shows the conversion in reverse direction from few-modes input 4M-WG to a single-mode output 1M-WG (i.e. fundamental mode) at the operating wavelength of 1550 nm. Fig. 4 (a)-(d) show the 2D cross-sections (in x-y directions) of 3D simulations for the cases of input 1$^{st}$ (fundamental), 2$^{nd}$, 3$^{rd}$, and 4$^{th}$ order modes, respectively. Here, the M-shape GI profile of M-MS is suitable to slice input TE2 or TE3 modes in two TE1 modes, each propagating like two parallel beams, without introducing distortions to the mode shape. The TE1 modes are sliced again to get four equal-power quarters, then their relative phase-differences are re-adjusted before re-combining them again to excite the fundamental mode in the output 1M-WG. It is worth mentioning that the mode-profiles in reverse direction show also good quality shapes and conversions as expected. Similarly, the case would be for conversion from 3M-WG to 1M-WG, so it is found to be sufficient showing the FDTD of 4M-WG case only.

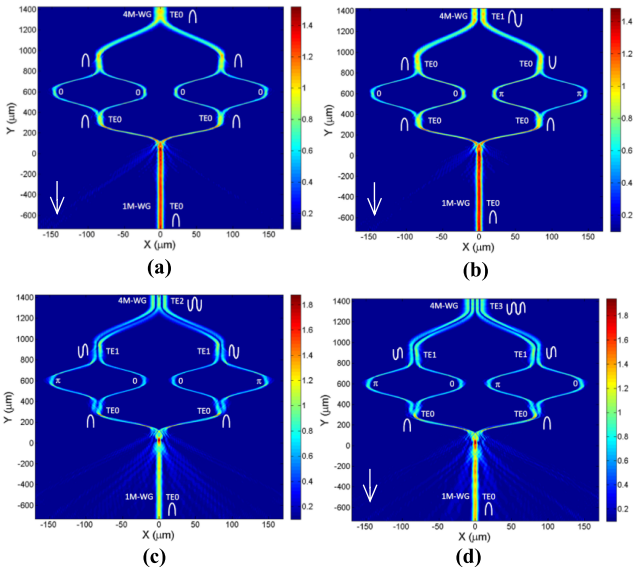


**FIGURE 4. The FDTD simulations of electric field magnitudes in a.u. (x-y cross-sections) for the case of WG conversion from 4M-WG to 1M-WG in reverse direction. The phase-shifters are adjusted in each case to convert from (a) TE0, (b) TE1, (c) TE2, and (d) TE3 of input 4M waveguide. The propagating modes are sketched at each stage. The white arrow on the lower-left corner indicates the propagation direction.**

The FDTD simulations here verify the bidirectional operation of WGC device to convert between the single-mode waveguide and 4-modes or 3-modes waveguides and vice-versa.

## III. PERFORMANCE EVALUATION

In order to assess the waveguide converter performance, the 3D FDTD simulations are performed over the C-band covering a wavelength range from 1.53 $\mu$m up to 1.565 $\mu$m. The device performance parameters (measured in decibels)

can be defined as: Insertion-loss (IL) = $-10\log_{10}$ ($P_o/P_i$), polarization-dependent-loss (PDL) = $IL_{TE} - IL_{TM}$, and return-loss (RL) = $-10\log_{10}$ ($P_{BR}/P_i$). Where '$P_i$' is the input power to WGC, '$P_o$' is the output power into the desired excited mode, '$P_{BR}$' is the back-reflected power from the input waveguide. The 'TE' and 'TM' are transverse-electric and magnetic polarizations, respectively.

Fig. 5 (a)-(c) show the performance of 1M-WG to 4M-WG WGC in bidirectional directions. The curves legends are shown in part (c). Fig. 5 (a) shows the IL for each exited mode in either output 4M-WG or 1M-WG. The worst case insertion loss is ≅ 3dB. Which is considered reasonable. The IL for TE2 and TE3 are higher than TE0 and TE1 because the former mandates excitation of TE1 mode, while the latter mandates excitation of TE0 mode in the 2M-WGs of the second stage, respectively. The TE1 mode in 2M-WGs suffers more radiation loss during excitation than TE0 because it has more mode field width. Fig. 5 (b) shows the PDL for each exited mode in either output 4M-WG or 1M-WG. The TE and TM polarizations are excited separately in the input waveguide, while the output insertion loss is estimated for each output excited mode in order to calculate the IL difference. The worst case PDL is ≅ 0.6dB. Which is considered also reasonable. Fig. 5 (c) shows the RL for each exited mode in either output 4M-WG or 1M-WG. The worst case return loss is ≅ 21dB at the wavelength of 1553nm. Which is also considered reasonable. Fig. 5 (d)-(f) show the performance of 1M-WG to 3M-WG WGC in bidirectional directions. The curves legends are shown in part (f). Fig. 5 (d) shows the IL for each exited mode in the output waveguide. The worst case insertion loss is ≅ 2.7dB. Fig. 5 (e) shows the PDL for each exited mode in the output waveguide. The worst case PDL is ≅ 0.45dB. Fig. 5 (f) shows the RL for each exited mode in the output waveguide. The worst case return loss is ≅ 21.3dB at a wavelength of ≅1550 nm. Which is also considered reasonable. These performance parameters evaluations indicate that bidirectional operations of the WGC device with 3M-WG or 4M-WG have good performance.

Although the performance in the forward and reverse directions are almost similar, it is worth mentioning that there might be some slight differences. That is because in the forward direction input power is divided among the desired and undesired modes in output few-mode waveguide. In other words, input power is distributed among several modes in the output waveguide. Whereas, in the reverse direction, one selected input mode is injected and its power is collected by only one mode in the output single-mode waveguide. So, it is expected to have such slight differences in estimated bidirectional performance.

Fig. 6 shows the estimated cross-talk (XT) in dB between the desired excited modes and undesired excited modes, for the two cases of output 4M-WG and 3M-WG over the entire C-band. To measure the XT, the phase-shifters of WGC are adjusted each time to selectively excite only one desired

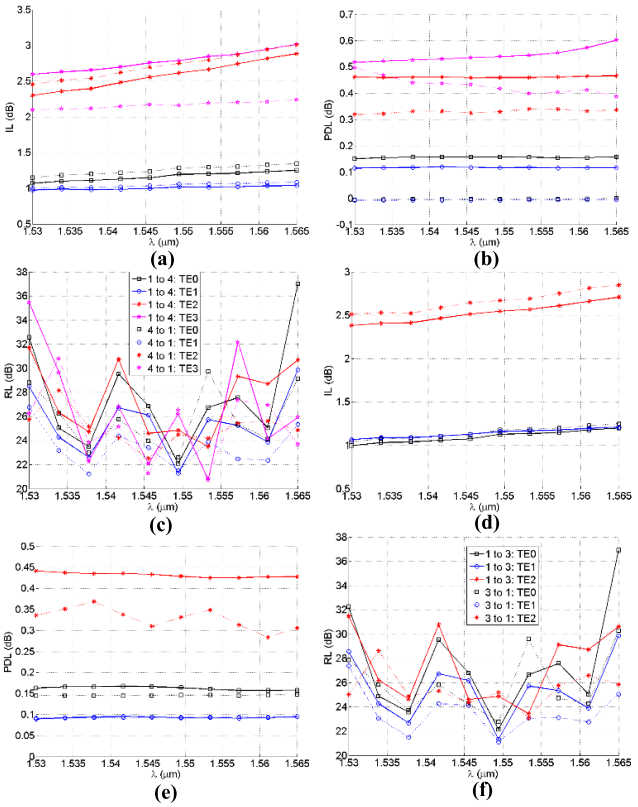


**FIGURE 5.** The performance evaluation of WGC parameters in bidirectional directions over C-band. In the case of conversion between 1M-WG and 4M-WG: (a) Insertion-loss, (b) Polarization-dependent loss, and (c) Return-loss together with figures legends. In the case of conversion between 1M-WG and 3M-WG: (d) Insertion-loss, (e) Polarization-dependent loss, and (f) Return-loss together with figures legends.

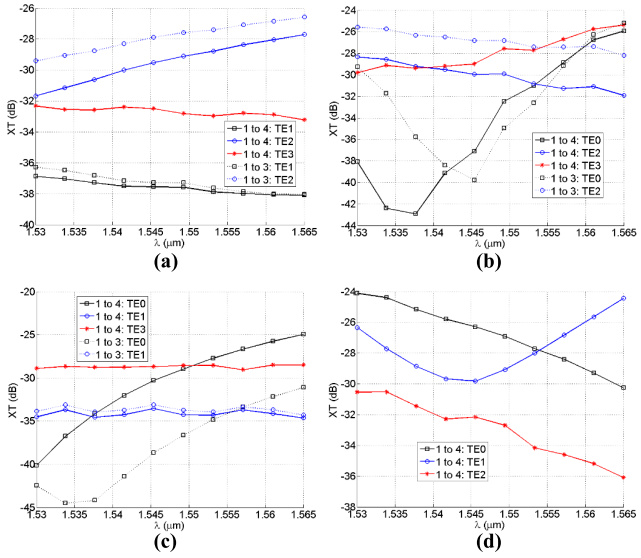


**FIGURE 6.** The estimated cross-talk (XT) between desirable and undesirable excited modes in 4M or 3M output waveguide, over the C-band, given the WGC is configured to excite only one target (desirable) mode. The desired target mode is: (a) TE0, (b) TE1, (c) TE2, and (d) TE3.

(target) mode in output WG, then the insertion loss is measured for this excited mode as well as for undesirable (unavoidable) excited modes. The insertion loss of undesirable modes is considered a cross-talk due to cross-coupling with the excited desirable modes. The XT expresses how well the desired output mode is excited without excitation of other undesired modes in the output waveguide. For 4M-WG case, the worst case XT across the C-band is found to be $\cong -24.1$dB for undesirable TE0 mode when the desired excited mode is TE3. Which is considered reasonable. The worst XT usually takes place between the excited even modes or odd modes. That is because the excitation of even modes requires the same width of M-MC ($178\mu$m), while excitation of odd modes requires another width of M-MC waveguide ($182\mu$m), as stated earlier. It is found that to minimize XT between even modes, it is better to excite TE0 at the zero cross-over locations of TE2 mode. However, to minimize XT between odd modes, it is better to excite TE1 at the zero cross-over locations of TE3 mode. For 3M-WG case, the worst case XT across C-band is found to be $\cong -25.5$dB for undesirable TE2 mode when the desired excited mode is TE1. Which is also considered reasonable.

Fig. 7 shows the estimated mode-rejection ratio (MRR) for conversion in reverse direction from input 4M-WG or 3M-WG modes to 1M-WG output fundamental mode. The phase-shifters of the WGC device are configured to selectively convert only one input desirable mode: TE0, TE1, TE2, and TE3 in Fig. 7 (a), (b), (c), and (d), respectively. For each configuration, the input waveguide mode is changed while keeping the phase shifters fixed in order to estimate the MRRs of such modes at the output waveguide. The MRR is estimated as the insertion loss for each input mode at one selected device configuration. The MRR expresses how well the undesired input modes are rejected (i.e. not converted to output 1M-WG mode), if the device is configured to convert another desired mode.

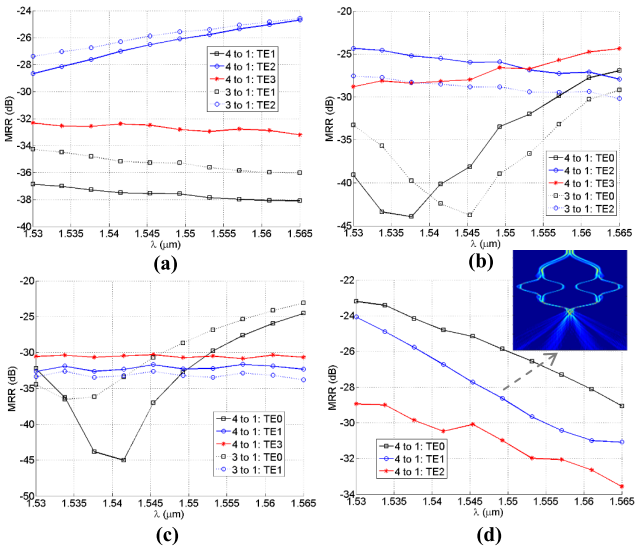


**FIGURE 7. The estimated mode-rejection ratio (MRR) for conversion from 4M-WG or 3M-WG input modes to 1M-WG output fundamental mode, over the C-band, given the WGC is configured to convert only one input desirable mode. The configured device mode is: (a) TE0, (b) TE1, (c) TE2, and (d) TE3. The inset shows an example of the FDTD electric field corresponding to one selected MRR value, as indicated by the arrow.**

The inset shows an example of 2D FDTD (x-y directions) electric field at the wavelength of 1550nm for input 4M-WG TE1 mode, when the device is configured for TE3 conversion. The MRR, in this case, is $\cong -28.8$dB. The worst case MRR over the entire C-band is found to be $\cong -23$dB at the wavelength of 1530nm for input 4M-WG TE0 mode, when the device is configured for TE3 conversion. Which is considered reasonable. For 3M-WG case, the worst case MRR is found to be $\cong -23$dB at the wavelength of 1560nm for input TE0 mode, when the device is configured for TE2 conversion. Which is also considered reasonable.

Fig. 6 and 7 indicate that bidirectional operation of the 3M and 4M WGC device has a good performance with respect to cross-talks and mode-rejection ratios.

## IV. PERFORMANCE TOLERANCE

In this section, the performance tolerances to design parameters are investigated and discussed. The limits of design parameters, over which the device can keep acceptable performance, set the design tolerance margins. These margins can help giving indications on the limits of fabrication errors, and the sensitivity to fabrication imperfections. For simplicity, the case of conversion from 1M-WG to 4M-WG at 1550nm is considered as an example to examine performance tolerances, because such conversion would be the worst case scenario.

The IL and XT are selected to be the most critical performance parameters to investigate. Because both can decide on how well the desired mode is excited with low loss and negligible crosstalk with undesirable modes. The worst-case unacceptable values of IL and XT are assumed to be 10dB and $-10$dB, respectively. Actually, the performance parameter (either IL or XT) that reaches the worst case first will set the limit on design parameters margins. The critical design parameters selected here are the length, width and graded-index slope of V-shape and M-shape waveguides, in addition to the separation 'd' between the centers of V-shaped diamond structures within the second stage. The variation in 'd' accounts for possible misalignments between the second stage and the first or third stage. More specifically, it represents possible misalignments between the diamond shapes and input/ output 2M-WGs of the first/ third stages (i.e. displacements of 2M-WGs from apex angle tip location). Such misalignments may, of course, introduce some power imbalance between V-MS and V-MC arms, and thus can affect the overall device performance.

Fig. 8 shows the performance tolerance to small changes in V-shape waveguides parameters (within the first and second stages) such as lengths ($\Delta L_V$), widths ($\Delta W_V$), graded-index slopes ($\Delta\alpha_V$), and separation between the 2$^{nd}$ stage diamond structures ($\Delta d_V$). The original length, width, slope, and separation of V-shape waveguides are almost $245\mu$m,

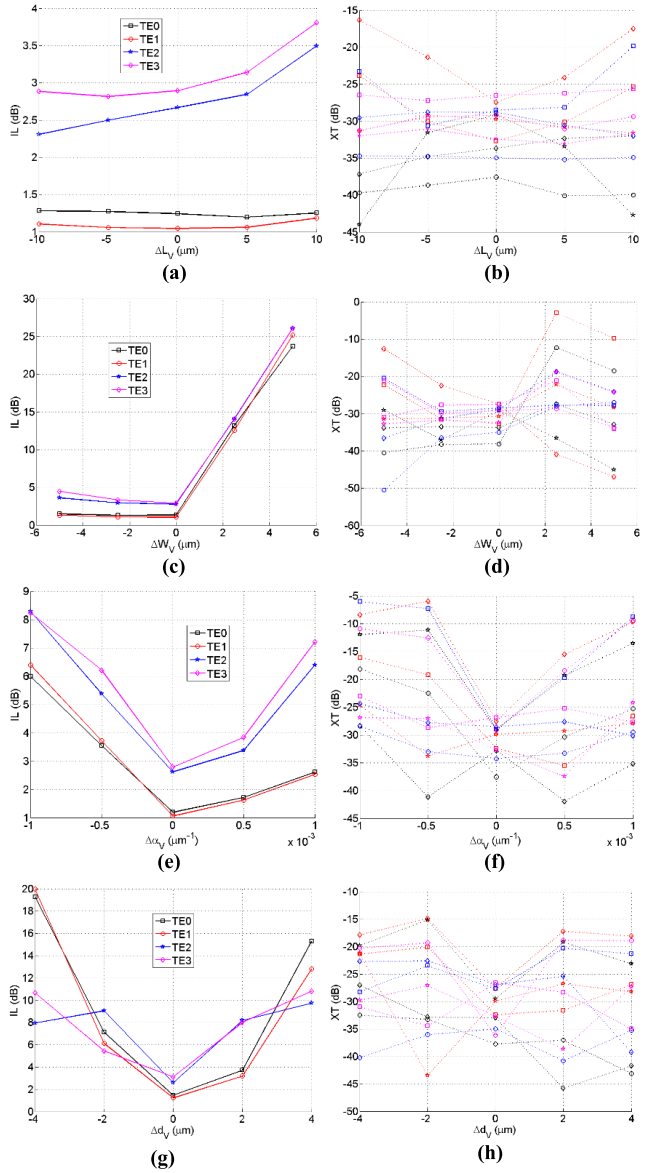


**FIGURE 8.** The performance tolerance to small variations in V-shape waveguides design parameters. The selected case is 1M-WG to 4M-WG conversion at the 1550nm operating wavelength. The left-column figures correspond to IL, while the right-column figures correspond to XT. The variations are in: (a-b) length '$\Delta L_V$', (c-d) width '$\Delta W_V$', (e-f) graded-index slope '$\Delta\alpha_V$', and (g-h) center-to-center separation between diamond structures of second stage '$\Delta d_V$'. In the right-column, black, red, blue, and magenta line-colors correspond to crosstalk with TE0, TE1, TE2, and TE3 modes, respectively. Whereas, squares, circles, pentagram-stars, and diamonds line-markers correspond to cross-talk with undesirable modes TE0, TE1, TE2, and TE3, respectively.

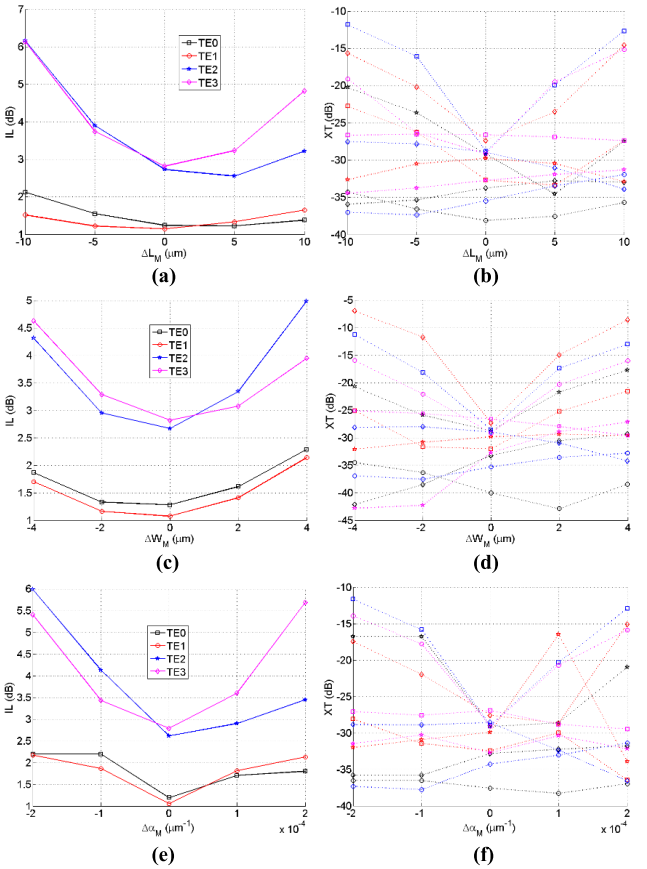


**FIGURE 9.** The performance tolerance to small variations in M-shape design parameters. The selected case is 1M-WG to 4M-WG conversion at 1550nm operating wavelength. The left-column figures correspond to IL, while the right-column figures correspond to XT. The variations are in: (a-b) length '$\Delta L_M$', (c-d) width '$\Delta W_M$', and (e-f) graded-index slope '$\Delta\alpha_M$'. In the right-column, black, red, blue, and magenta line-colors correspond to crosstalk with TE0, TE1, TE2, and TE3 modes, respectively. Whereas, squares, circles, pentagram-stars, and diamonds line-markers correspond to cross-talk with undesirable modes TE0, TE1, TE2, and TE3, respectively.

35$\mu$m, 3.1x10$^{-2}\mu$m$^{-1}$, and 168$\mu$m, respectively. For each design parameter variations, the changes in IL are shown for all possible excited modes (TE3, TE2, TE1, and TE0) on the left-column figures. Whereas, the changes in XT with undesirable modes are shown on the right-column figures. In Fig. 8 (a) and (b), $\Delta L_V$ is varied between $-10$ and $+10\mu$m. The maximum IL is just below 4dB, while the maximum XT is just below $-15$dB, for all modes. Thus, the device shows a very good performance over the tested range $\Delta L_V \cong \pm 10\ \mu$m, which is considered $\cong \pm 4.1\%$ of designed and optimized $L_V$ value. In Fig. 8 (c) and (d), the IL of all modes exceeds 10dB when the V-shape width reaches 2dB. Whereas the XT exceeds $-10$ dB when $\Delta W_V$ is $\cong 2$ or $-5\ \mu$m (i.e. $\cong 5.7$ or $-14.3\%$). In Fig. 8 (e) and (f), The XT exceeds $-10$dB at $\Delta\alpha_V = 1x10^{-3}$ and $-0.4x10^{-3}\mu m^{-1}$ (i.e. $\cong 3.2$ and $-1.3\%$). While IL is acceptable ($<$10dB) for $\Delta\alpha_V = \pm 1x10^{-3}\ \mu m^{-1}$ (i.e. $\cong \pm 3.2\%$). In Fig. 8 (g) and (h), the IL exceeds 10dB when $\Delta d_V \cong \pm 2.5\ \mu$m (i.e. $\cong \pm 1.5\%$), while the XT remains reasonable within this range. Which indicates that the device can withstand an introduced power imbalance between diamond-shape arms due to input/ output waveguides misalignments up to $\pm 2.5\ \mu$m, while keeping an acceptable performance.

All the above values indicate reasonable performance tolerances to variations in V-shape waveguides design parameters.

Fig. 9 shows the performance tolerance to small changes in M-shape waveguide parameters (within the third stage) such as length ($\Delta L_M$), width ($\Delta W_M$), and graded-index slope ($\Delta\alpha_M$). For each design parameter variations, the changes in

IL are shown for all possible excited mode (TE3, TE2, TE1, and TE0) on the left-column figures. Whereas, the changes in XT with undesirable modes are shown on the right-column figures. In Fig. 9 (a) and (b), both IL and XT remain reasonable within the tested range $\Delta L_M \cong \pm 10\,\mu$m (i.e. $\cong \pm 2.7\%$). In Fig. 9 (c) and (d), The XT exceeds $-10$dB when $\Delta W_M \cong -2.5$ or $3.5\,\mu$m (i.e. $\cong -1.4$ and $1.9\%$). In Fig. 9 (e) and (f), both IL and XT remain reasonable within the tested range of $\Delta\alpha_M \approx \pm 2x10^{-4}\mu m^{-1}$ (i.e. $\cong \pm 2.4\%$). All these values indicate reasonable performance tolerances to variations in design parameters of M-shape waveguide design parameters.

## V. CONCLUSIONS

A novel planar silica-glass few-modes waveguide converter is proposed and numerically demonstrated for the first time. It can convert in bidirectional directions between single mode and two, three, or four modes waveguides. Such waveguide conversion can be considered a first step to generate higher or lower order modes before multiplexing or demultiplexing in mode-division multiplexing applications. The device operation depends on spatial slicing and combining of modes using V-shape and M-shape graded-index profiles. The device shows a good performance in both directions over the entire C-band wavelength range ($\cong$ 35nm). The worst-case insertion-loss, polarization-dependent loss, and return-loss are $\cong$ 3, 0.6, and 21dB, respectively. While, the worst-case cross-talk and mode-rejection ratio are $\cong -24.1$dB and $-23$dB, respectively. The performance tolerances to V-shape and M-shape waveguides design parameters variations prove to be reasonable, which in turn relax the constraints on device fabrication errors and sensitivity margins. Although the device fabrication is not the main focus in this paper here, it is worth mentioning that there are various fabrication methods to realize PIC silica-glass planar waveguides [20], and also some special fabrication techniques [21], [22] could be utilized to realize the peak indices within these silica-glass waveguides.

## ACKNOWLEDGMENT

The author would like to gratefully acknowledge the technical support from the Research Center at the College of Engineering, and the Deanship of Scientific Research at King Saud University.

## REFERENCES

[1] H. Takahashi, "High performance planar lightwave circuit devices for large capacity transmission," *Opt. Express*, vol. 19, pp. B173–B180, Dec. 2011.
[2] C. R. Doerr and K. Okamoto, "Advances in silica planar lightwave circuits," *J. Lightw. Technol.*, vol. 24, no. 12, pp. 4763–4789, Dec. 2006.
[3] I. Ogawa *et al.*, "Packaging technology for ultra-small variable optical attenuator multiplexer (V-AWG) with multichip PLC integration structure using chip-scale-package PD array," *IEEE J. Sel. Topics Quantum Electron.*, vol. 12, no. 5, pp. 1045–1053, Sep. 2006.
[4] H. Takahashi, "Planar lightwave circuit devices for optical communication: present and future," *Proc. SPIE*, vol. 5246, pp. 520–531, Aug. 2003.
[5] K. Watanabe, Y. Hashizume, Y. Nasu, M. Kohtoku, M. Itoh, and Y. Inoue, "Ultralow power consumption silica-based PLC-VOA/switches," *J. Lightw. Technol.*, vol. 26, no. 14, pp. 2235–2244, Jul. 15, 2008.
[6] M. Kawachi, "Silica waveguides on silicon and their application to integrated-optic components," *Opt. Quantum Electron.*, vol. 22, no. 5, pp. 391–416, 1990.
[7] E. Awad, "Multicore optical fiber Y-splitter," *Opt. Express*, vol. 23, no. 20, pp. 25661–25674, 2015.
[8] E. Awad, "V-splitter with adjustable power splitting ratio," *Opt. Quantum Electron. J.*, vol. 49, no. 9, p. 300, 2017.
[9] W. Y. Chan and H. P. Chan, "Two-mode mode multiplexer/demultiplexer in polymer planar waveguide," *Appl. Opt.*, vol. 53, pp. 496–502, Jan. 2014.
[10] C. Sun, Y. Yu, G. Chen, and X. Zhang, "Integrated switchable mode exchange for reconfigurable mode-multiplexing optical networks," in *Proc. 42nd Eur. Conf. Opt. Commun. (ECOC)*, Dusseldorf, Germany, Sep. 2016, pp. 1–3.
[11] B.-T. Lee and S.-Y. Shin, "Mode-order converter in a multimode waveguide," *Opt. Lett.*, vol. 28, no. 18, pp. 1660–1662, 2003.
[12] J. D. Love and N. Riesen, "Single-, few-, and multimode Y-junctions," *J. Lightw. Technol.*, vol. 30, no. 3, pp. 304–309, Feb. 1, 2012.
[13] M. Ye, Y. Yu, C. Sun, and X. Zhang, "On-chip data exchange for mode division multiplexed signals," *Opt. Express*, vol. 24, no. 1, pp. 528–535, 2016.
[14] B. Stern *et al.*, "On-chip mode-division multiplexing switch," *Optica*, vol. 2, pp. 530–535, Jun. 2015.
[15] Y. Ding, J. Xu, F. Da Ros, B. Huang, H. Ou, and C. Peucheret, "On-chip two-mode division multiplexing using tapered directional coupler-based mode multiplexer and demultiplexer," *Opt. Express*, vol. 21, no. 8, pp. 10376–10382, 2013.
[16] K. Chen *et al.*, "Experimental demonstration of simultaneous mode and polarization-division multiplexing based on silicon densely packed waveguide array," *Opt. Lett.*, vol. 40, pp. 4655–4658, Oct. 2015.
[17] D. Dai, J. Wang, and Y. Shi, "Silicon mode (de)multiplexer enabling high capacity photonic networks-on-chip with a single-wavelength-carrier light," *Opt. Lett.*, vol. 38, no. 9, pp. 1422–1424, 2013.
[18] B. E. A. Saleh and M. C. Teich, *Fundamentals of Photonics*, 2nd ed. Hoboken, NJ, USA: Wiley, 2007.
[19] Lumerical Solutions. Accessed: 2018. [Online]. Available: https://www.lumerical.com
[20] G. C. Righini and A. Chiappini, "Glass optical waveguides: a review of fabrication techniques," *Opt. Eng.*, vol. 53, no. 7, p. 071819, 2014.
[21] D. Duchesne *et al.*, "Efficient self-phase modulation in low loss, high index doped silica glass integrated waveguides," *Opt. Express*, vol. 17, pp. 1865–1870, Feb. 2009.
[22] D. J. Moss, R. Morandotti, A. L. Gaeta, and M. Lipson, "New CMOS-compatible platforms based on silicon nitride and hydex for nonlinear optics," *Nature Photon.*, vol. 7, pp. 597–607, Aug. 2013.

**EHAB AWAD** received the B.Sc. degree in electrical engineering from Cairo University, Egypt, and the M.Sc. and Ph.D. degrees in electrical engineering from the University of Maryland at College Park, USA. He is currently a Professor at the Electrical Engineering Department, King Saud University, Saudi Arabia. His research interests include optoelectronics devices, optical communications, nano-plasmonics, optical fibers, and infrared sensors. He is a Senior Member of the IEEE Photonics Society and the Optical Society of America.